

REPORT DOCUMENTATION PAGE				Form Approved OMB No. 0704-0188	
<p>The public reporting burden for this collection of information is estimated to average 1 hour per response, including the time for reviewing instructions, searching existing data sources, gathering and maintaining the data needed, and completing and reviewing the collection of information. Send comments regarding this burden estimate or any other aspect of this collection of information, including suggestions for reducing the burden, to Department of Defense, Washington Headquarters Services, Directorate for Information Operations and Reports (0704-0188), 1215 Jefferson Davis Highway, Suite 1204, Arlington, VA 22202-4302. Respondents should be aware that notwithstanding any other provision of law, no person shall be subject to any penalty for failing to comply with a collection of information if it does not display a currently valid OMB control number.</p> <p><b>PLEASE DO NOT RETURN YOUR FORM TO THE ABOVE ADDRESS.</b></p>					
1. REPORT DATE (DD-MM-YYYY) 01-07-2010		2. REPORT TYPE Journal Article		3. DATES COVERED (From - To)	
4. TITLE AND SUBTITLE  Pore-scale study of the collector efficiency of nanoparticles in packings of nonspherical collectors				5a. CONTRACT NUMBER	
				5b. GRANT NUMBER	
				5c. PROGRAM ELEMENT NUMBER	
				5d. PROJECT NUMBER	
6. AUTHOR(S)  Wei Long, Haiou Huang, Jasmine Serlemitos, Elizabeth Liu, Allen H. Reed, Markus Hilpert				5e. TASK NUMBER	
				5f. WORK UNIT NUMBER 74-7632-07	
				7. PERFORMING ORGANIZATION NAME(S) AND ADDRESS(ES) Naval Research Laboratory Marine Geoacoustics Division Stennis Space Center, MS 39529	
9. SPONSORING/MONITORING AGENCY NAME(S) AND ADDRESS(ES)  Office of Naval Research 800 North Quincy Street Arlington VA 22217-5000				B. PERFORMING ORGANIZATION REPORT NUMBER NRL/JA/7430-07-10	
				10. SPONSOR/MONITOR'S ACRONYM(S) ONR	
12. DISTRIBUTION/AVAILABILITY STATEMENT  Approved for public release; distribution is unlimited				11. SPONSOR/MONITOR'S REPORT NUMBER(S)	
				13. SUPPLEMENTARY NOTES Colloids and Surfaces A: Physicochem. Eng. Aspects 358 (2010) 163-171	
14. ABSTRACT  Pore-scale simulations of flow and transport through a filter were used to predict clean-bed filtration of nanoparticles from a 3D image of the filter. X-ray micro-computed tomography was used to obtain the geometry and topology of the filter consisting of flattened half-spherical collectors. A Lattice-Boltzmann method was used to model fluid flow and particle transport in the volumetric image of the filter. Nanoparticles are considered that are so small that diffusion, as compared to the processes of gravitational settlement and interception, dominates particle deposition. A correlation equation is determined for the average collector efficiency for diffusion through regression analysis performed for a set of numerical breakthrough experiments for a range of suspended particle sizes and Darcy velocities. This correlation quantifies the collector size by the surface average equivalent sphere diameter. The newly derived correlation agrees well with experimental data.					
15. SUBJECT TERMS  Filtration, Nanoparticle, Collector efficiency, Lattice-Boltzmann, Pore-scale, Nonspherical collector					
16. SECURITY CLASSIFICATION OF:			17. LIMITATION OF ABSTRACT  UU	18. NUMBER OF PAGES  9	19a. NAME OF RESPONSIBLE PERSON Allen Reed
a. REPORT Unclassified	b. ABSTRACT Unclassified	c. THIS PAGE Unclassified			19b. TELEPHONE NUMBER (Include area code) 228-688-5473

20100923480



## Pore-scale study of the collector efficiency of nanoparticles in packings of nonspherical collectors

Wei Long<sup>a,\*</sup>, Haiou Huang<sup>b</sup>, Jasmine Serlemitsos<sup>a</sup>, Elizabeth Liu<sup>a</sup>, Allen H. Reed<sup>c</sup>, Markus Hilpert<sup>a</sup>

<sup>a</sup> Johns Hopkins University, Department of Geography and Environmental Engineering, 313 Ames Hall, 3400 N. Charles St., Baltimore, MD 21218, United States

<sup>b</sup> Johns Hopkins Bloomberg School, Public Health Center for Water and Health, 615 N Wolfe St., Baltimore, MD 21205, United States

<sup>c</sup> Naval Research Laboratory, 1005 Balch Blvd., Stennis Space Center, MS 39520, United States

### ARTICLE INFO

#### Article history:

Received 31 July 2009

Received in revised form 15 January 2010

Accepted 20 January 2010

Available online 25 January 2010

#### Keywords:

Filtration

Nanoparticle

Collector efficiency

Lattice-Boltzmann

Pore-scale

Nonspherical collector

### ABSTRACT

Pore-scale simulations of flow and transport through a filter were used to predict clean-bed filtration of nanoparticles from a 3D image of the filter. X-ray micro-computed tomography was used to obtain the geometry and topology of the filter consisting of flattened half-spherical collectors. A Lattice-Boltzmann method was used to model fluid flow and particle transport in the volumetric image of the filter. Nanoparticles are considered that are so small that diffusion, as compared to the processes of gravitational settlement and interception, dominates particle deposition. A correlation equation is determined for the average collector efficiency for diffusion through regression analysis performed for a set of numerical breakthrough experiments for a range of suspended particle sizes and Darcy velocities. This correlation quantifies the collector size by the surface average equivalent sphere diameter. The newly derived correlation agrees well with experimental data.

© 2010 Elsevier B.V. All rights reserved.

### 1. Introduction

Nano-sized particle transport provides solutions, concerns and potential hazards. For instance, the use of manufactured nanoparticles in groundwater remediation is a new and promising technology [15,47]. The discharge of nanoparticles during remediation, however, poses a potential risk to public health [25,36]. Moreover, the transport of viruses/pathogens with sizes on the order of nanometers in saturated porous media is receiving more and more attention [34,3,37]. These facts demonstrate the need to investigate the fate and transport of nanoparticles, including particle deposition, in natural and engineered porous media.

Particle deposition has been conceptualized to occur in two steps [13,12]: (1) transport of the suspended particles to a collector surface by advection and diffusion as quantified by the collector efficiency  $\eta_0$  [–]; and (2) attachment of the particles to the collector surface by interaction forces as quantified by the collision efficiency  $\alpha$  [–]. One can use  $\alpha$  and  $\eta_0$  to model the deposition term in the following macro-scale equation for particle transport in a sphere

packing during clean-bed filtration [17]:

$$\frac{\partial c}{\partial t} + \bar{\nabla} \cdot (\bar{v}c) = \bar{\nabla} \cdot (\mathbf{D}_m \bar{\nabla} c) - \frac{3}{2} \frac{1-\varepsilon}{d_c} \alpha \eta_0 |v| c \quad (1)$$

where  $c$  [kg/m<sup>3</sup>] is the particle concentration,  $t$  is the time,  $\bar{v}$  [m/s] is the pore-water velocity,  $\mathbf{D}_m$  [m<sup>2</sup>/s] is a tensor that accounts for hydrodynamic dispersion and molecular diffusion,  $\varepsilon$  [–] is the porosity, and  $d_c$  [m] is the grain (collector) diameter. The first term on the left hand side of the equation describes particle accumulation. The second term describes advective transport. The first term on the right hand side of the equation describes particle transport that does not occur with the mean pore-water velocity, and the second term describes particle deposition.

Because of the computational cost of pore-scale simulations of particle transport in a representative elementary volume (REV) of a filter, unit-cell approaches have been traditionally employed to derive correlation equations for  $\eta_0$ . Such unit-cell approaches, for example, represent a filter of spherical collector particles by (1) an isolated spherical collector that is surrounded by a laminar flow field of infinite extent [45], or (2) Happel's sphere-in-cell model [19], a single collector that is surrounded by an imaginary spherical shell in which laminar flow takes place with hypothetical boundary conditions for fluid velocity and particle concentration [33,40].

The aforementioned unit-cell approaches have the following shortcomings:

\* Corresponding author.

E-mail address: [longwei.usa@yahoo.com](mailto:longwei.usa@yahoo.com) (W. Long).



## Nomenclature

### List of symbols

$c$	particle concentration (kg/m <sup>3</sup> )
$C_n$	distribution function for particle concentration
$d_c$	diameter of collectors (m)
$d_p$	diameter of particles (m)
$D_c$	surface average equivalent sphere diameter (m)
$\mathbf{D}_m$	diffusion/dispersion tensor (m <sup>2</sup> /s)
$\mathbf{D}_p$	particle diffusion tensor (m <sup>2</sup> /s)
$f_n$	distribution function for fluid density
$g$	gravitational acceleration (m/s <sup>2</sup> )
$k$	Boltzmann constant (J/K)
$L$	height/length of the column (m)
$N_{Pe}$	Peclet number
$N_R$	interception number
$p$	pressure (Pa)
$S_c$	surface area of a collector (m <sup>2</sup> )
$\Delta t$	time step (s)
$T$	temperature (K)
$U$	superficial velocity or Darcy velocity (m/s)
$\bar{v}$	pore-water velocity (m/s)
$v_0$	$\Delta x/\Delta t$ (m/s)
$V_c$	collector volume (m <sup>3</sup> )
$\Delta x$	lattice spacing (m)
$\alpha$	collision efficiency
$\eta_0$	collector efficiency
$\eta_D$	diffusion collector efficiency
$\eta_{corr}$	collector efficiency from correlation (16)
$\eta_{sim}$	collector efficiency from numerical simulations
$\eta_{exp}$	collector efficiency from experiments
$\varepsilon$	porosity
$\nu$	kinematic viscosity (m <sup>2</sup> /s)
$\sigma$	surface charge density (μC/cm <sup>2</sup> )
$\rho_p$	particle density (kg/m <sup>3</sup> )
$\rho_f$	fluid density (kg/m <sup>3</sup> )
$\tau_f, \tau_c$	relaxation times for fluid and particles, respectively

- Correlation equations based on single-collector approaches do not accurately account for the complex flow and concentration fields in real porous media, because real pore geometries and topologies are much more complicated than those of unit cells.
- Even if a correlation equation based on a single-collector model is deemed to be sufficient, existing single-collector models are limited in their ability to describe filtration in packings of non-spherical collectors, with a notable exception in which [35] used a unit-cell approach to study the influence of collector shape and roughness on  $\eta_0$ .

In order to better represent the topology of a filter pore space, simulations in pore networks have been used to investigate filtration in porous media [6,38]. These simulations partition the pore space into smaller elements (pore bodies and pore throats) and simulate transport in each of these elements using simple algebraic rules for the incoming and outgoing particle concentrations.

It is, however, difficult to make quantitative predictions from a 3D image of a porous medium using current pore-network modeling approaches for particle filtration, because they do not represent the topology of the porous medium.

Due to continuously increasing CPU speeds and the availability of massive parallel computers, Lattice-Boltzmann (LB) methods [43,10] have become attractive for performing pore-scale simulations of a broad range of transport phenomena in porous media. The LB method addresses complex pore geometries within parallel computational platforms, which in turn allows the simulation of large domains. LB methods have been used to simulate fluid flow (e.g. [30]) and small particle transport (e.g. [23]) in porous media.

Few LB studies have, however, investigated filtration. Przekop et al. [32] studied particle deposition in fibrous filters. Lin and Miller [26] investigated the flow field during filtration. Baumann and Werth [4] compared flow paths and particle velocities in a micro-model to a 2D LB model. Chen et al. [7] studied the permeability reduction due to colloid deposition by combining X-ray tomography and pore-scale LB simulations. Long and Hilpert [27] developed a correlation equation for an average single-collector efficiency for clean-bed filtration in sphere packings.

The objective of this paper is to demonstrate that pore-scale simulations (and in particular an LB method) of flow and transport can be used to predict clean-bed filtration of nanoparticles from a 3D image of the filter, which consists of collectors that are too non-spherical to apply correlation equations for  $\eta_0$  that have been developed for spherical collectors (e.g. [33,40,27]). For instance, clay particles are not spherical, and sand and gravel particles are not perfect spheres. Also manufactured filters do not always consist of spherical collector particles. This work considers collectors that resemble flattened half spheres. We will further consider filtration of nanoparticles that are so small that diffusion, as compared to the processes of gravitational settlement and interception, dominates particle deposition. Hence,  $\eta_0$  can be approximated by the diffusion collector efficiency  $\eta_D$ . In the experimental portion of this paper, (1) a column filled with flattened half spheres is imaged using X-ray micro-computed tomography to obtain the geometry and topology of the packing in 3D, and (2) clean-bed filtration experiments are performed in this column using nanoparticles. In the theoretical portion of the paper, (1) a LB method is used to model particle transport in the 3D image of the filter, (2) a correlation equation for  $\eta_D$  for nanoparticle filtration is developed from a regression analysis of a set of numerical breakthrough experiments, and (3) the prediction of the correlation equation is compared to the column experiments obtained for  $\alpha = 1$ . We also comment on the column experiments that were performed under unfavorable attachment conditions,  $\alpha < 1$ .

## 2. Experimental methods

### 2.1. Particle suspension

For the nanoparticles/suspensions, we used four types of surfactant-free polystyrene latex particles (Interfacial Dynamics Corporation, Portland, OR), each of which has a relatively uniform size distribution (see Table 1). The 120-nm Latex A particles contain amidine groups on their surfaces, and therefore, have a positive

**Table 1**  
Some properties of the nanoparticles used in our experiments.

Label	Diameter from TEM by manufacturer	Diameter from PCS from our measurements	Surface charge density, $\sigma$
Latex A	120 ± 17 nm	134 nm	+8.1 μC/cm <sup>2</sup>
Latex B	19 ± 3 nm	28 nm	−2.4 μC/cm <sup>2</sup>
Latex C	43 ± 7 nm	57 nm	−1.7 μC/cm <sup>2</sup>
Latex D	93 ± 5 nm	109 nm	−2.2 μC/cm <sup>2</sup>



surface charge density  $\sigma$ . The Latex B, C, and D nanoparticles contain sulfate groups and have negative surface charge densities in the entire pH range used in this study. The particle density  $\rho_p$  is 1.055 g/cm<sup>3</sup> for all particles as reported by the manufacturer. Particle diameters were measured by the manufacturer using transmission electron microscopy (TEM). These values, however, are smaller than the ones obtained in this study, which uses photon correlation spectroscopy (PCS) of suspensions of the nanoparticles in distilled water (Brookhaven Instruments Corporation). In PCS, the hydrodynamic diameter  $d_p$  is inferred from the measurement of the mean diffusion coefficient of the suspended particles and the Einstein–Stokes equation. We used the particle sizes determined by PCS as model inputs due to their relevance to particle transport in aqueous phase.

## 2.2. Porous media

About uniform-sized non-spherical beads with an approximate shape of flattened half spheres (supplied by Atofina/Arkema chemical company) are used as the collectors in the deposition experiments. The about half-sphere shape is due to the manufacturing process, during which soft spherical PVDF beads, created from a PVDF melt, deformed and flattened due to the action of gravity before complete solidification. The beads are made of polyvinylidene fluoride (PVDF, Kynar® 460). Polyvinylidene fluoride resin was chosen due to its relevance in environmental technology such as membrane-based water treatment. The density of the PVDF beads measured by the manufacturer is 1.688 g/cm<sup>3</sup>. The size in the largest dimension is about 5 mm. The surface charge of the PVDF beads was not determined in this study but is expected to be slightly negative according to streaming potential measurements on a microfiltration membrane, which was fabricated from similar materials, in distilled water [24]. A X-ray photon spectrometry (XPS) analysis was conducted and showed that the surface composition of Kynar® 461 (powder form of Kynar® 460) is almost exclusively C<sub>2</sub>H<sub>2</sub>F<sub>2</sub>. Oxygen is not detected at a noticeable level, indicating the absence of hydroxyl or other oxygen-containing ionizable groups on the surfaces of the beads. The beads were rinsed extensively with ultrapure water generated by a MilliQ water system (Millipore) before the filtration experiments. In order to explore favorable chemical conditions ( $\alpha = 1$ ) for Latex A particles, deposition experiments were also performed using PVDF beads which were immersed in a solution with sodium dodecyl sulfate (SDS) for 4 h, and the results were compared to experiments using PVDF beads without SDS coating.

## 2.3. Solution chemistry

In all of the experiments, the buffer solution consists of 1 mM of CaCl<sub>2</sub> to control ionic strength, and 0.1 mM of NaHCO<sub>3</sub> to maintain the pH at 7.5. For the tracer breakthrough experiments, NaNO<sub>3</sub> is added at a concentration of 0.1 mM as a tracer. All chemicals used are reagent grade.

## 2.4. Deposition experiment

A cylindrical column with an inside diameter of 2.54 cm and a height of 29.3 cm is used in the deposition experiments. Fresh PVDF beads are densely packed in this column prior to each experiment. The measured average porosity of the entire bead packing was 43%. Particle suspensions with a concentration of 2 mg/L were prepared by adding latex stock suspensions to the aforementioned buffer solutions and sonicating them for 1 h to break up any aggregates. Aggregation of latex particles at different calcium concentrations was studied in a series of jar tests. Addition of 1 mM of CaCl<sub>2</sub> did not cause noticeable turbidity increase in the time frame of the fil-

tration experiment, indicating stability of the particles with respect to aggregation. The packed column was first flushed with five pore volumes of ultrapure water, followed by flushing with another five pore volumes of the buffer solution. Then the latex suspension was pumped through the column. The effluent particle concentration was continuously monitored by a UV spectrophotometer equipped with a flow-through cuvette (Shimadzu UV-160). Linear correlations between particle/tracer concentration and UV absorbance at a wavelength of 220 nm (for particles) and 305 nm (for tracer) were determined in preliminary experiments. The influent was switched to the buffer solution after 3–5 pore volumes of the particle suspension. The filtration experiment was finally stopped after flushing with another 3–4 pore volumes of buffer solution. Three different flow rates were employed in the filtration of positively charged particles: 6.2, 3.2, and 1.5 mL/min, corresponding to Darcy velocities of 17.6, 9.1, 4.3 m/d, respectively. For the negatively charged particles, we tested the same three flow rates. The differences in effluent concentration for these three flow rates were, however, relatively small such that we could not observe how flow rate affects particle deposition. To better resolve this dependency, we used flow rates of 6.2, 1.5 and 0.37 mL/min, corresponding to Darcy velocities of 17.6, 4.3 and 1.1 m/d, respectively, for the negatively charged particles. Note that the Darcy velocities used in the experiments are higher than those typically observed for groundwater flow, but they can be representative for filtration during water treatment. During each filtration experiment, the flow rate remained constant. All experiments were conducted at room temperature, 25 °C.

## 2.5. Micro-computed tomography

We obtained high-resolution volumetric images of the filtration column by using non-destructive X-ray micro-computed tomography, as used in many other areas, including soil science [2] and hydrology [42]. We used a microfocus X-ray computed tomography (MXCT) system. Our MXCT produces polychromatic X-rays with an acceleration potential ranging from 10 to 225 keV and an electrical current ranging from 0 to 3 mA. During a CT scan, X-rays are projected from a cone-beam onto and through the sample, which is located between the X-ray source and the detector (a charge-coupled device or CCD). The sample is rotated by 360° at predetermined angular increments. X-ray attenuation depends on the sample density, atomic number, and column diameter. Provided a sufficient number of X-rays pass through the sample to the detector, a series of two-dimensional (2D) horizontal images (or CT “slices”) are produced using the Feldkamp algorithm [16] from the X-ray attenuation data, which was collected at 2400 angular increments during sample rotation. These 2D images, which are accurately aligned in the vertical dimension, are converted into a volumetric image during post-processing. The cone-beam captures the full diameter of the sample column, but because the height of a sample column is often longer than the diameter of the X-ray beam, the sample is translated vertically and scanned again. The process of translating the sample vertically and then scanning it is repeated until the desired sample length is imaged.

## 3. Theoretical methods

### 3.1. Simulation of fluid flow by the LB method

To simulate filtration, first the fluid velocity field is determined. At the pore scale, the Navier–Stokes equation,

$$\frac{\partial \vec{v}}{\partial t} + \vec{v} \cdot \nabla \vec{v} = -\frac{1}{\rho_f} \nabla p + \nu \nabla^2 \vec{v} + \vec{g} \quad (2)$$



describes fluid flow, where  $\vec{v}$  is the pore-scale velocity field,  $p$  [Pa] is pressure,  $\nu$  [m<sup>2</sup>/s] is the kinematic viscosity,  $\rho_f$  [kg/m<sup>3</sup>] is the fluid density, and  $\vec{g}$  [m/s<sup>2</sup>] is the gravitational acceleration vector.

The LB method represents the fluid particles by quasi particles that travel along a typically regular numerical lattice and collide at the lattice nodes. We used the LB model described in [22] for solving the Navier–Stokes equation (2) numerically. This model uses a three-dimensional cubic lattice with 15 velocity vectors (a D3Q15 model with 6 velocities along the lattice axes, 8 along the space diagonals, and 1 zero vector for rest particles). The LB equation for single-phase flow can be written as

$$f_n(\vec{x}_i + \vec{e}_n, t + 1) - f_n(\vec{x}_i, t) = \Omega_n \quad (3)$$

where  $f_n$  is the distribution function for the fluid,  $\Omega_n$  is the collision term, and  $n = 0, \dots, 14$  specifies the velocity vector. The left hand side of Eq. (3) describes the travel (streaming) step, and the right hand side describes the collision step. We use a single-relaxation-time model for the collision term:

$$\Omega_n = \frac{1}{\tau_f} [f_n^{(0)}(\vec{x}_i, t) - f_n(\vec{x}_i, t)] \quad (4)$$

where  $\tau_f$  is the relaxation time of the fluid which is related to the fluid viscosity by

$$\tau_f = \frac{1}{2} + 3 \frac{\nu}{\Delta x v_0} \quad (5)$$

$v_0 = \Delta x / \Delta t$ ,  $\Delta x$  is the lattice spacing,  $\Delta t$  is the time step,

$$f_n^{(0)} = \gamma_n \hat{\rho} \left[ 1 + 3 \hat{V} \cdot \vec{e}_n + \frac{9}{2} (\hat{V} \cdot \vec{e}_n)^2 - \frac{3}{2} \hat{V}^2 \right] \quad (6)$$

is the equilibrium distribution function for the fluid,  $\gamma_0 = 2/9$ ,  $\gamma_n = 1/9$  for  $n = 1, \dots, 6$ ,  $\gamma_n = 1/72$  for  $n = 7, \dots, 14$ ,  $\hat{\rho} = \sum_{i=0}^{14} f_i$  is the nondimensional fluid density, which is related to the nondimensional pressure by  $\hat{p} = \hat{\rho}/3$ , and  $\hat{V} = \sum_{i=0}^{14} f_i \vec{e}_i / \hat{\rho}$  is the nondimensional fluid velocity. See the appendix in [22] for a derivation that shows that the LB method simulates fluid flow fields which satisfy the Navier–Stokes equation.

In a LB simulation, one can induce flow by applying either a body force or a pressure gradient [8,10]. A body force requires periodic boundary conditions which do not occur in the experiment. We generate a 0.1% pressure (density) difference between the inlet and the outlet to induce flow. Fluid flows in the vertical direction, i.e. upward. The velocity field is then retrieved from the simulations at steady-state. This velocity field is used as an input to the particle transport model described next.

### 3.2. Simulation of particle transport and deposition by the LB method

An advection–diffusion equation [11] describes particle transport at the pore scale

$$\frac{\partial c}{\partial t} + \vec{\nabla} \cdot (\vec{v}c) = \vec{\nabla} \cdot (\mathbf{D}_p \vec{\nabla} c) - \vec{\nabla} \cdot \left( \frac{\mathbf{D}_p \vec{F}}{kT} c \right) \quad (7)$$

where  $k$  [J/K] is the Boltzmann constant,  $T$  [K] is the absolute temperature,  $\vec{F}$  [N] is the external force on the particles (e.g. gravity and DLVO forces), and  $\mathbf{D}_p$  [m<sup>2</sup>/s] is the particle diffusion tensor. In our simulations, gravity is the only external force. We do not account for the lubrication effect [31] and anisotropic diffusion [1], both of which are accounted for in the correlation equation by [40] for clean-bed filtration in sphere packings. Even though this latter correlation was developed for sphere packings, we could actually use it to estimate the effects of lubrication and anisotropic diffusion on particle transport in our packings of flattened half spheres. We found that these effects should affect  $\eta_D$  only marginally [27].

As we do not account for anisotropic diffusion, the diffusion tensor becomes a scalar quantity which can be estimated from the Einstein–Stokes equation,

$$D = \frac{kT}{3\pi\rho_f \nu d_p} \quad (8)$$

where  $d_p$  [m] is the diameter of the suspended spherical particles.

Our LB method uses the same numerical lattice for particle transport as is used for modeling fluid flow (D3Q15). The LB equation for particle transport is

$$C_n(\vec{x}_i + \vec{e}_n, t + 1) - C_n(\vec{x}_i, t) = \frac{1}{\tau_c} [C_n^{(0)}(\vec{x}_i, t) - C_n(\vec{x}_i, t)] \quad (9)$$

where  $C_n$  [–] is the distribution function for the suspended particles, and  $\tau_c$  [–] is the relaxation time for the suspended particles which is related to the lattice Peclet number  $Pe_c$  by

$$\frac{1}{Pe_c} = \frac{D}{\Delta x v_0} = \frac{\tau_c}{3} - \frac{1}{6} \quad (10)$$

If the external force in Eq. (7) accounts for gravity and buoyancy, then the nondimensional advection–diffusion equation can be approximated by the LB equation (9) with an equilibrium distribution function given by [27]

$$C_n^{(0)} = \beta_n \hat{c} [1 + 3 \hat{e}_n \cdot (\hat{V} + \hat{V}_s)] \quad (11)$$

where  $\beta_0 = 2/9$ ,  $\beta_n = 1/9$  for  $n = 1, \dots, 6$ ,  $\beta_n = 1/72$  for  $n = 7, \dots, 14$ ,  $\hat{c} = \sum_{i=0}^{14} C_i$  [–] is the nondimensional particle concentration,

$$\hat{V}_s = \frac{(\rho_p - \rho_f) g d_p^2}{18 \rho_f \nu v_0} \quad (12)$$

is the nondimensional particle settling velocity, and  $\rho_p$  [kg/m<sup>3</sup>] is the particle density.

Through a Chapman and Enskog expansion, we can show that the concentration fields obtained from the LB equation (9) with the equilibrium distribution functions given by Eq. (11) do approximate the ones from the nondimensional advection–diffusion equation [20]. Moreover, our modeling approach [27] accounts for all of the three transport mechanisms, diffusion, interception and gravitation, which according to [45], contribute to particle filtration.

### 3.3. Development of a correlation equation for $\eta_D$

We performed numerical column breakthrough experiments in the 3D pore structure of the volumetric X-ray CT image and inferred  $\eta_D$  from the steady-state effluent concentration  $c_{out}$ . We first simulated the steady-state pore-scale velocity field in the scanned porous medium. Then, we used this velocity field as an input to our LB model for particle transport. We applied the Dirichlet boundary condition at the inlet of the column,  $c(x, y, z = 0, t) = c_{in}$ , where  $c_{in}$  is the concentration of the suspended particles injected into the column. At the outlet, we used the Neumann boundary condition,  $\partial c(x, y, z = L, t) / \partial z = 0$ . The perfect-sink boundary condition,  $c = 0$ , at the collector surface could be applied to obtain  $\alpha = 1$  since  $d_p \ll d_c$ . When deriving a correlation equation for  $\eta_D$ , we could assume that interception and gravitation had negligible impact on  $\eta_D$ , i.e.  $\eta_D \approx \eta_0$ , because particle size  $d_p$  was very small. The collector efficiency  $\eta_0$  can then be determined from [44,45]

$$\eta_D = -\frac{2}{3} \frac{d_c}{(1 - \varepsilon)L} \ln \left( \frac{c_{out}}{c_{in}} \right) \quad (13)$$

Eq. (13) is obtained by solving Eq. (1) using the assumptions that flow is one-dimensional and at steady-state, and longitudinal hydrodynamic dispersion, which occurs at the Darcy scale, does not significantly affect particle transport [45].



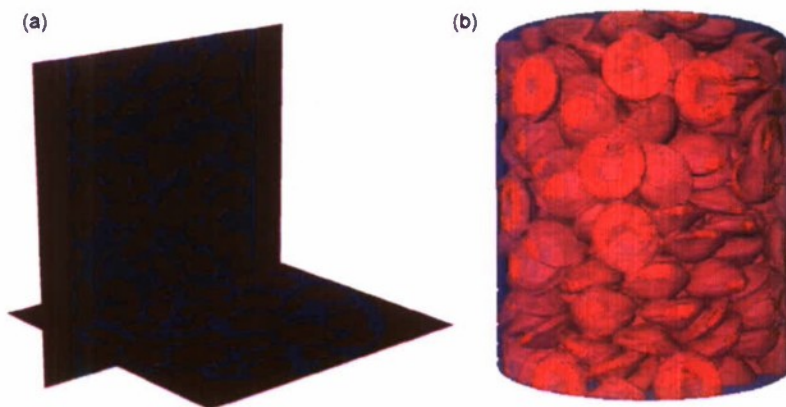


Fig. 1. CT images of the packing. (a) A vertical and horizontal slice. The red represents the solid phase, and the blue represents the pore space. (b) 3D view.

For nonspherical grains such as our collector particles, the surface average equivalent sphere diameter,  $D_c$  [m], is often used to specify their size:

$$D_c = \frac{6V_c}{S_c} \quad (14)$$

where  $V_c$  [m<sup>3</sup>] is the grain volume, and  $S_c$  [m<sup>2</sup>] is the surface area of the grain. We can determine  $V_c$  and  $S_c$  from the volumetric CT images. As we neglect the lubrication effect and van der Waals forces (we do not include  $N_{vdw}$  in our correlation), we assume the correlation for  $\eta_D$  to be a function of the porosity,  $f(\varepsilon)$ , the interception number,  $N_R = d_p/D_c$ , and the Peclet number  $N_{Pe} = UD_c/D$  where  $U$  is the Darcy velocity. We use the expression  $f(\varepsilon) = (1 - \varepsilon)^3 / \varepsilon^2$  to model the porosity dependence of  $\eta_D$ . Such a porosity dependence has also been used in a previous study [27] on the collector efficiency of packings of spheres. The concentration limits,  $c_{out} = 0$  for  $\varepsilon = 0$  and  $c_{out} = c_{in}$  for  $\varepsilon \rightarrow 1$ , are properly captured by our  $f(\varepsilon)$ . Thus,  $\eta_D$  can be written as

$$\eta_D = c_1 \frac{(1 - \varepsilon)^3}{\varepsilon^2} N_{Pe}^{c_2} N_R^{c_3} \quad (15)$$

The coefficients  $c_1$ ,  $c_2$ , and  $c_3$  in Eq. (15) can be determined from a multivariate regression analysis on the  $\eta_D$  values obtained from a set of the numerical breakthrough experiments in the volumetric CT image of the filter material.

## 4. Results and discussion

### 4.1. Experimental results from X-ray CT

We imaged a middle layer of the entire column. The MXCT was operated with an acceleration potential of 100 keV and an electrical current of 80  $\mu$ A. The sample stage was set 65 cm from the X-ray source. This setup enabled the X-ray beam to span the 2.54 cm in diameter sample and allowed X-rays to reach the detector at a sufficient intensity. After each scan of the sample, the sample was translated vertically to scan a desired sample height. Given this setup, the sample was imaged in the  $x$ ,  $y$ , and  $z$ -directions with a resolution of 0.05045 mm. Given the number of voxels per particle diameter, this resolution provides an accurate representation of the PVDF beads; accurate representation of similar particles has been determined to occur for 10–20 voxels per particle diameter with accuracy increasing as the number of voxels per particle diameter increases [39].

The entire image of the middle layer consists of  $519 \times 519 \times 533$  voxels. MXCT images are 16-bit gray-scale images. A good image contrast was obtained due to the X-ray attenuation difference

between the flattened half spheres and the surrounding air. While the gray-scale histogram of the MXCT image has two distinct peaks, one for the flattened half spheres and one for the surrounding pore space, a percentage of voxels has intermediary values, which are difficult to assign to a given population using a simple thresholding technique. Therefore, an indicator kriging algorithm was employed to convert the entire MXCT image into a 1-bit binary image. This algorithm is used to assign voxels that clearly belong to the flattened half spheres a value of 1 and to assign voxels that clearly belong to the pore space a value of 0. The intermediary values are assigned a value of 1 or 0 depending upon the gray-scale values of the neighboring voxels [28]. Porosity is then readily determined by taking the sum of the 0's divided by the total number of voxels in the image. Fig. 1 shows that the resulting image provides a realistic geometry that resolves the orientation of the PVDF beads and also the contact points between the beads.

Through image analysis, we determined that the middle layer had a porosity of 38%. This porosity is lower than the average column porosity (43%), indicating that the beads were not uniformly packed. Ideally, we should have scanned the entire column to identify a region, in which the porosity was about equal to the average column porosity of 43%, and then used this region in the filtration simulation. It was, however, unrealistic to scan the entire column due to the cost of the MXCT measurements. In order to account for the difference in porosity, we used the porosity of the middle layer when determining the parameters of the correlation equation (15) from the LB simulations, because this porosity corresponds to the simulation domain. When predicting  $\eta_D$  of the entire column, however, we used the porosity of the entire column in our correlation equation.

### 4.2. Results for deposition experiments

Using the strategy explained in [14], we experimentally determined conditions for which  $\alpha = 1$ . The idea is that any particle colliding with a collector will attach to it, if the collectors and the particles are oppositely charged. Such experiments are performed at a relatively high ionic strength in order to avoid  $\alpha > 1$ , that is, deposition enhancement due to attractive van der Waals forces [9]. To prevent particle aggregation, excessively high ionic strengths (>5 mM) are avoided.

We conducted particle deposition experiments with the positively charged Latex A particles. Since pristine PVDF collectors are possibly only slightly negatively charged due to the lack of ionizable function groups on PVDF structures, coating the collectors with the surfactant SDS, which possesses a negatively charged sulfate group, should increase the zeta potential and the surface charge

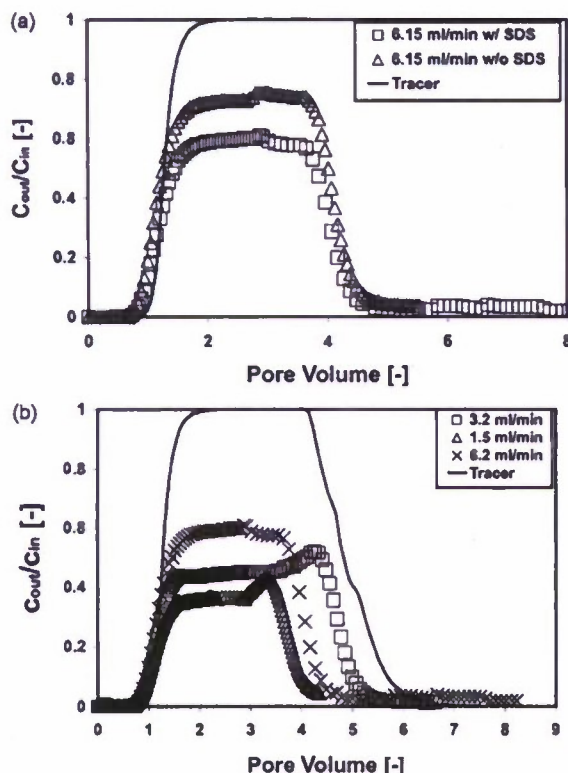


Fig. 2. Particle breakthrough curves for Latex A particles: (a) PVDF beads either coated or not coated with surfactant (SDS). (b) PVDF beads are coated with SDS; use of three different flow rates.

density of the collectors [24]. To determine the conditions for which  $\alpha = 1$ , we obtained breakthrough curves with the collectors either being coated with SDS or not. We used a  $\text{CaCl}_2$  solution with an ionic strength of 1 mM to prevent  $\alpha > 1$ . The breakthrough curves in Fig. 2(a) show that  $\alpha$  is higher for the SDS coated collectors. Thus, we concluded that the SDS coated collectors yielded  $\alpha = 1$ . Using the SDS coated collectors, a set of triplicate deposition experiments was performed for three different flow rates. Fig. 2(b) illustrates the flow rate dependence of the breakthrough curves.

#### 4.3. Modeling results

To determine the coefficients in Eq. (15) we first inferred  $D_c$  from the volumetric CT image. We used a pore-space analysis software

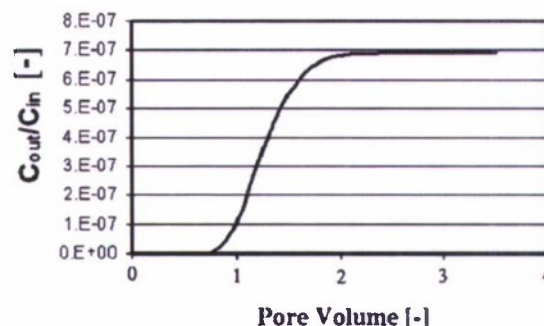


Fig. 4. Numerical breakthrough curve for the simulation illustrated in Fig. 3.

[18] to determine the average surface area of a collector,  $S_c$ , from the CT image. Likewise, the collector volume,  $V_c$ , was calculated from the segmented CT image. Using Eq. (14), we obtained  $D_c = 3.6$  mm.

Because of the computational expense filtration was simulated in subdomains of the volumetric CT image. Due to the randomness of the pore structure,  $\eta_D$  differs for different subdomains of the porous medium, even if porosity  $\varepsilon$  is the same, as we also found in a study on filtration in sphere packings [27]. The mean value of  $\eta_D$  is expected to remain approximately constant, while the variation in  $\eta_D$  is expected to decrease, as the domain size increases. The domain size has reached a representative elementary volume (REV), once the variation becomes negligible. To account for the possibility that the volumes of the subdomains are smaller than a REV, we identified four different subdomains, all of which have about the same porosity,  $\varepsilon = 0.38 \pm 0.01$ . The subdomains consist of  $250 \times 250 \times 200$ ,  $250 \times 250 \times 200$ ,  $200 \times 200 \times 300$ , and  $200 \times 200 \times 400$  voxels and contain between 80 and 105 flattened half-spherical collectors. The subdomains have slightly different volumes in order to ensure that their four  $\varepsilon$  values fall into the prescribed  $\varepsilon$  interval.

In these four subdomains, we performed a set of numerical breakthrough experiments for different values of  $U$  and  $d_p$ . Fig. 3 illustrates how the particle concentration develops during such a numerical experiment. The breakthrough curve is shown in Fig. 4. For each value of  $U$  and  $d_p$ , we obtained four different  $\eta_D$  values, from which we calculated an average  $\eta_D$  value. Those average values were then used to develop a correlation equation for  $\eta_D$ . We determined the coefficients in Eq. (15) through regression analysis and obtained

$$\eta_D = (8.34 \pm 0.75) \frac{(1 - \varepsilon)^3}{\varepsilon^2} N_{Pe}^{-0.53 \pm 0.015} N_R^{-0.03 \pm 0.0175} \quad (16)$$

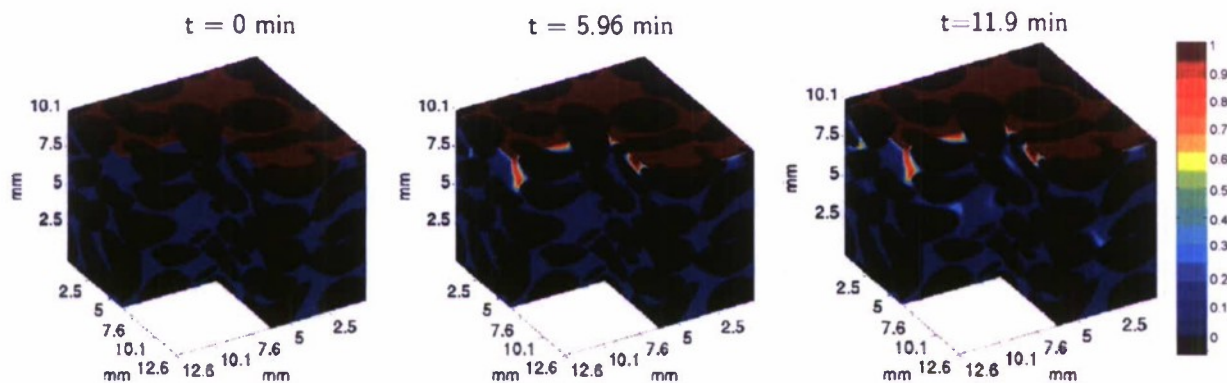


Fig. 3. Particle concentration at selected times  $t$  in a packing of flattened half spheres. The color represents the particle concentration and the black represents the solid phase. Note that fluid flows from  $z = 0$  to  $z = 1.01$  cm while the simulation results are displayed oppositely to give a better visualization. Simulation parameters:  $U = 0.025$   $\mu\text{m/s}$ ,  $\varepsilon = 0.38$ ,  $d_p = 20$  nm, and  $L = 1.01$  cm.



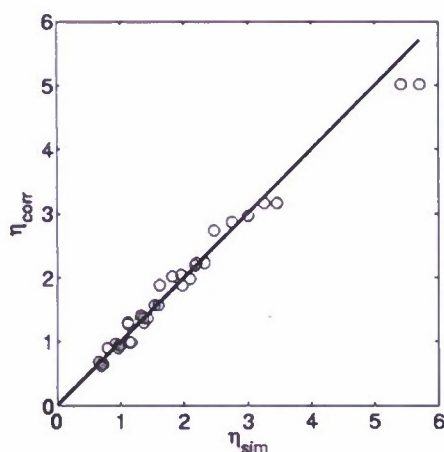


Fig. 5. Comparison of the collector efficiency from the numerical simulations with the predictions from the correlation for the four different subdomains and for different values of  $U$  and  $d_p$ . Simulation parameters:  $D_c = 3.6$  mm,  $\varepsilon = 0.43$ ,  $L = 1.01$  mm, and  $\Delta x = 50.48$   $\mu$ m.

Table 2  
Summary of parameters used in numerical simulations.

Parameter	Range
$d_p$	0.02–1 $\mu$ m
$\varepsilon$	0.38
$U$	0.025–1 $\mu$ m/s
$T$	298 K
$k$	$1.38 \times 10^{-23}$ J/K
$D_c$	3.6 mm
$\rho_p$	1.055 g/cm <sup>3</sup>

Fig. 5 compares the collector efficiency inferred via Eq. (13) from individual numerical breakthrough experiments,  $\eta_{sim}$ , with the predictions based on the correlation equation (16),  $\eta_{corr}$ . The good agreement between  $\eta_{sim}$  and  $\eta_{corr}$  demonstrates the appropriateness of the functional form of our correlation for  $\eta_D$ . A correlation coefficient of  $R = 0.98$  illustrates the good fit. Table 2 summarizes the parameters used in the simulations.

Note that the velocities we used in our simulation vary from 0.002 to 0.1 m/d and are smaller than the ones we used in the experiments. This is due to numerical instability which would occur for high Peclet numbers or high flow rates. Due to the relatively small Peclet numbers used in the simulations, the simulated nondimensional breakthrough concentrations are small too (see Fig. 4). Even though the correlation equation that we developed for  $\eta_D$  is based on simulations with small Peclet numbers, the correlation equation can be used to predict filtration experiments performed at higher Peclet numbers as demonstrated in a similar study on filtration in sphere packings [27]. As in [27] we will use statistical methods to quantify the extrapolation error.

We can also comment on the REV for filtration in a packing of flattened half spheres, even though this study has not been specifically designed to determine this REV. To that end, we would have needed to simulate filtration for a wide range of domains sizes, as in LB studies of permeability [5,46,29] or in pore-morphology

Comparison of the Experiments with the Correlation

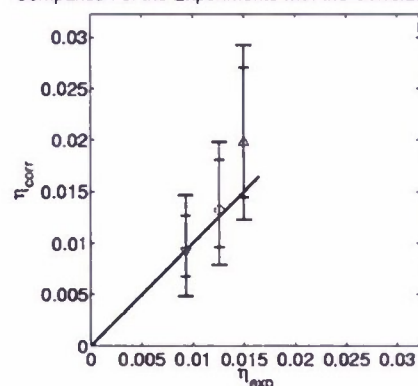


Fig. 6. Comparison of the collector efficiency from the correlation and the experiments for Latex A particles for three different flow rates: 6.2 mL/min ( $\nabla$ ), 3.2 mL/min ( $\circ$ ), and 1.5 mL/min ( $\Delta$ ).

based modeling studies of primary drainage [21]. We can, however, examine the statistics of  $\eta_D$  for the simulations in the four statistically identical subdomains. A possible definition of REV relates to the domain volume, at or above which the relative standard deviation of the variable of interest is smaller than a user-specified percentage, for example, 5% in the permeability study by [29]. Table 3 shows that the relative standard deviation of  $\eta_D$  is a function of both Darcy velocity  $U$  and particle size  $d_p$ . The relative standard deviation increases with decreasing  $d_p$  and increasing  $U$  values. Our simulation domain would constitute a REV for all  $d_p$  and  $U$  values presented, if one accepted a 10% standard deviation. If one accepted a 5% standard deviation, then our simulation domain would be a REV only for  $d_p$  above 200 nm and  $U$  below  $2.5 \times 10^{-8}$  m/s. Hence, depending on the accepted standard deviation, our simulation domains may constitute a REV or not. We accounted for the latter possibility by having performed filtration simulations in four different subdomains of the imaged packing of flattened half spheres that all have the same porosity  $\varepsilon$ . Simulations in bigger domains would be desirable and are expected to yield smaller error bounds for the coefficients in our correlation equation (16).

Note that our correlation equation given by Eq. (16) accounts explicitly for the porosity  $\varepsilon$ . However, the correlation equation is based on simulations in packings with a single porosity of 38%. We have neither experimental nor numerical data to support the porosity dependence posited in Eq. (16). Additional investigations are necessary to test the porosity term in Eq. (16). We did not perform these investigations due to the cost of obtaining CT scans.

#### 4.4. Comparison of $\eta_D$ between the correlation equation and the experiments

Fig. 6 compares the collector efficiency measured in the experiments,  $\eta_{exp}$ , with the prediction calculated from our correlation equation (16),  $\eta_{corr}$ . The  $\eta_{exp}$  values reflect the mean values from the triplicate deposition column experiments that we performed for the three different flow rates. In order to evaluate the pre-

Table 3  
Statistics of the  $\eta_D$  values simulated in statistically identical packings of flattened half spheres.

$d_p$ (nm)	Relative standard deviation of $\eta_D$ (constant $U = 2.5 \times 10^{-8}$ m/s)	$U$ (m/s)	Relative standard deviation of $\eta_D$ (constant $d_p = 100$ nm)
20	8.42%	$2.47 \times 10^{-8}$	4.95%
50	7.86%	$6.17 \times 10^{-8}$	7.51%
100	5.72%	$1.23 \times 10^{-7}$	8.72%
200	1.45%	$2.47 \times 10^{-7}$	9.93%



**Table 4**

Removal efficiency for three different nanoparticle sizes and three different flow rates in deposition experiments.

Particle label	Flow rate (mL/min)	Porosity, $\varepsilon$ (%)	$1 - c_{out}/c_{in}$ (%)	$\alpha$ [-]
Latex B	0.35	43	79	0.24
Latex B	1.5	43	63	0.32
Latex B	6.15	43	46	0.42
Latex C	0.39	43	71	0.28
Latex C	1.53	43	55	0.38
Latex C	6.15	43	40	0.51
Latex D	0.37	43	70	0.25
Latex D	1.5	43	45	0.27
Latex D	6.1	43	34	0.39

dictive capability of Eq. (16), we quantified the uncertainties of both the prediction from the correlation equation and the measured values. The smaller of the two overlapping vertical error bars represents the 95% confidence interval of the prediction of the correlation equation. In statistical terms, this is the confidence interval for the mean response [41, Ch. 12]. If the experimental measurement was without error, then this error bar should intersect with the one-to-one line for the correlation to explain the experimental data. This is the case for all the three data points. The mean experimental  $\eta_{exp}$  values have, however, some error, which we quantified by the 95% confidence interval of the mean. Hence, the prediction of the correlation equation may deviate from the one-to-one line by this confidence interval. In other words, the sum of the errors from the correlation and the experimental measurement should intersect with the one-to-one line. The bigger of the two overlapping vertical error bars represents this combined error. As these combined errors, and even the confidence intervals of the mean response alone, overlap with the one-to-one line, we can conclude that the correlation agrees well with the results of the column experiments. Correlation equations developed for spherical collectors [45,40,33] do not and cannot be expected to agree well with our experimental measurements (comparison not presented) because of the difference between spherical and our about half-spherical collectors.

Our comparison between the experimental data and our correlation equation is hampered by the fact that our column was not packed uniformly as exemplified by a spatially variable porosity. Hence, the measured collector efficiency,  $\eta_{exp}$ , should depend not only on porosity but also on the porosity variation. We could not quantify the effect that a non-uniform porosity has on  $\eta_0$ , but we expect the dependence of  $\eta_0$  on the porosity variation to be a correction to the dependence on  $\varepsilon$ ,  $N_{pe}$ , and  $N_R$ . Additional investigations, which would involve scanning entire filtration columns and testing them for uniform porosity, are necessary to resolve this issue.

We also examined whether our assumption of clean-bed filtration was justified. To that end, we assumed that all particles are deposited onto the collector surfaces during the entire filtration event and estimated the volume of particle deposited. Using a mass balance, we calculated a reduction in porosity by 0.00019% when flushing a column with one pore volume of nanoparticle-laden solution. In the experiments, the columns were flushed with 4–6 pore volumes. Hence, the porosity was reduced at most by about 0.001%. This small number justifies the assumption of clean-bed filtration.

#### 4.5. Application of the correlation to predict $\alpha$

The negatively charged Latex B, C, and D particles (see Table 1) used together with the negatively charged collectors (without SDS coating) yield unfavorable chemical conditions with respect to particle deposition (significantly lower  $\alpha$  values). For these unfavorable

conditions, the collision efficiency  $\alpha$  was calculated as follows [45]:

$$\alpha = -\frac{1}{\eta_0} \frac{2}{3} \frac{d_c}{(1-\varepsilon)L} \ln \left( \frac{c_{out}}{c_{in}} \right) \quad (17)$$

where Eq. (16) was employed for  $\eta_0$ . Table 4 summarizes  $\alpha$  and the removal efficiency  $1 - c_{out}/c_{in}$  for the three particle sizes and three different flow rates. As predicted by colloid filtration theory [45], the removal efficiency increases as the flow rate and particle size decrease, because in this nanoparticle experiments, particle deposition is governed by diffusion while gravitational settlement is negligible.

#### Acknowledgments

We thank Professor Charles R. O'Melia for discussion and direction, Professor Hugh Ellis for computing resources at Johns Hopkins University, Dr. Roland Glantz for his help on the calculation of surface area, Atofina/Arkema chemical company for donating the Kynar samples used in the experiments, and Kevin Wilson for assistance with image processing. We also thank the ONR Coastal Geosciences Program for funding for the CT work. MH was supported by NSF Grant EAR-0911425.

#### References

- [1] Z. Adamczyk, T. Dabros, J. Czarnecki, T.G.M. Vandeven, Particle transfer to solid-surfaces, *Advances in Colloid and Interface Science* 19 (1983) 183–252.
- [2] S.H. Anderson, R.L. Peyton, C.J. Gantzer, Evaluation of constructed and natural soil macropores using X-ray computed tomography, *Geoderma* 46 (1–3) (1990) 13–29.
- [3] R.C. Bales, S.M. Li, K.M. Maguire, M.T. Yahya, C.P. Gerba, Ms-2 and poliovirus transport in porous media – hydrophobic effects and chemical perturbations, *Water Resources Research* 29 (4) (1993) 957–963.
- [4] T. Baumann, C.J. Werth, Visualization and modeling of polystyrol colloid transport in a silicon micromodel, *Vadose Zone Journal* 3 (2) (2004) 434–443.
- [5] W.J. Bosl, J. Dvorkin, A. Nur, A study of porosity and permeability using a Lattice-Boltzmann simulation, *Geophysical Research Letters* 25 (9) (1998) 1475–1478.
- [6] V.N. Burganos, E.D. Skouras, C.A. Paraskeva, A.C. Payatakes, Simulation of the dynamics of depth filtration of non-Brownian particles, *AIChE Journal* 47 (4) (2001) 880–894.
- [7] C. Chen, A.J. Packman, J.F. Gaillard, Pore-scale analysis of permeability reduction resulting from colloid deposition, *Geophysical Research Letters* 35 (7) (2008), art. no. L07404.
- [8] H. Chen, S. Chen, W.H. Matthaeus, Recovery of the Navier-Stokes equations using a lattice-gas Boltzmann methods, *Physical Review A* 45 (1992) 5339–5342.
- [9] K.L. Chen, S.E. Mylon, M. Elimelech, Aggregation kinetics of alginate-coated hematite nanoparticles in monovalent and divalent electrolytes, *Environmental Science & Technology* 40 (2006) 1516–1523.
- [10] S. Chen, G.D. Doolen, Lattice-Boltzmann method for fluid flows, *Annual Review of Fluid Mechanics* 30 (1998) 329–364.
- [11] M. Elimelech, Particle deposition on ideal collectors from dilute flowing suspensions: mathematical formulation, numerical solution, and simulations, *Separations Technology* 4 (1994) 186–212.
- [12] M. Elimelech, C.R. O'Melia, Kinetics of deposition of colloidal particles in porous media, *Environmental Science & Technology* 24 (10) (1990) 1528–1536.
- [13] M. Elimelech, C.R. O'Melia, Effect of particle size on collision efficiency in the deposition of Brownian particles with electrostatic energy barriers, *Langmuir* 6 (6) (1990) 1153–1163.
- [14] M. Elimelech, J. Gregory, X. Jia, R. Williams, Modeling of particle deposition onto ideal collectors, in: R.A. Williams (Ed.), *Particle Deposition and Aggregation*, Butterworth-Heinemann Ltd., Linacre House, Jordan Hill, Oxford OX2 8DP, 1995, pp. 113–154.
- [15] D.W. Elliott, W.X. Zhang, Field assessment of nanoscale biometallic particles for groundwater treatment, *Environmental Science and Technology* 35 (24) (2001) 4922–4926.
- [16] L.A. Feldkamp, L.C. Davis, J.W. Kress, Practical cone-beam algorithm, *Journal of the Optical Society of America* 1 (6) (1984) 612–619.
- [17] T.R. Ginn, B.D. Wood, K.E. Nelson, T.D. Scheibe, E.M. Murphy, T.P. Clement, Processes in microbial transport in the natural subsurface, *Advances in Water Resources* 25 (2002) 1017–1042.
- [18] R. Glantz, M. Hilpert, Tight dual models of pore spaces, *Advances in Water Resources* 31 (2008) 787–806.
- [19] J. Happel, Viscous flow in multiparticle systems—slow motion of fluids relative to beds of spherical particles, *AIChE Journal* 4 (1958) 197–201.
- [20] M. Hilpert, Lattice-Boltzmann model for bacterial chemotaxis, *Journal of Mathematical Biology* 51 (2005) 302–332.
- [21] M. Hilpert, C.T. Miller, Pore-morphology-based simulation of drainage in totally wetting porous media, *Advances in Water Resources* 24 (3–4) (2001) 243–255.

- [22] S. Hou, Q. Zou, S. Chen, G. Doolen, A.C. Cogley, Simulation of cavity flow by the Lattice-Boltzmann method, *Journal of Computational Physics* 118 (1995) 329–347.
- [23] Q.J. Kang, P.C. Lichtner, D.X. Zhang, Lattice-Boltzmann pore-scale model for multicomponent reactive transport in porous media, *Journal of Geophysical Research-Solid Earth* 111 (B5) (2006).
- [24] K.J. Kim, A.G. Fane, M. Nystrom, A. Pihlajamaki, W.R. Bowen, H. Mukhtar, Evaluation of electroosmosis and streaming potential for measurement of electric charges of polymeric membranes, *Journal of Membrane Science* 116 (2) (1996) 149–159.
- [25] X.Q. Li, D.W. Elliott, W.X. Zhang, Zero-valent iron nanoparticles for abatement of environmental pollutants: materials and engineering aspects, *Critical Reviews in Solid State and Materials Sciences* 31 (4) (2006) 111–122.
- [26] C.L. Lin, J.D. Miller, Pore structure analysis of particle beds for fluid transport simulation during filtration, *International Journal of Mineral Processing* 73 (2–4) (2004) 281–294.
- [27] W. Long, M. Hilpert, A correlation for the collector efficiency of Brownian particles in clean-bed filtration in sphere packings by a Lattice-Boltzmann method, *Environmental Science and Technology* 43 (2009) 4419–4424.
- [28] W. Oh, W.B. Lindquist, Image thresholding by indicator kriging, *IEEE Transactions on Pattern Analysis and Machine Intelligence* 21 (1999) 590–602.
- [29] C. Pan, M. Hilpert, C.T. Miller, Pore-scale modeling of saturated permeabilities in random sphere packings, *Physical Review E* 64 (6) (2001) 066702.
- [30] C. Pan, M. Hilpert, C.T. Miller, Lattice-Boltzmann simulation of two-phase flow in porous media, *Water Resources Research* 40 (2004) W01501.
- [31] D.C. Prieve, M.M.J. Lin, Adsorption of Brownian hydrosols onto a rotating-disk aided by a uniform applied force, *Journal of Colloid and Interface Science* 76 (1980) 32–47.
- [32] R. Przekop, A. Moskal, L. Gradon, Lattice-Boltzmann approach for description of the structure of deposited particulate matter in fibrous filters, *Journal of Aerosol Science* 34 (2) (2003) 133–147.
- [33] R. Rajagopalan, C. Tien, Trajectory analysis of deep-bed filtration with the sphere-in-cell porous media model, *AIChE Journal* 22 (1976) 523–533.
- [34] L.L.C. Rehmann, C. Welty, Stochastic analysis of virus transport in aquifers, *Water Resources Research* 35 (7) (1999) 1987–2006.
- [35] J.E. Saiers, J.N. Ryan, Colloid deposition on non-ideal porous media: the influence of collector shape and roughness on the single-collector efficiency, *Geophysical Research Letters* 32 (21) (2005), art. no. L21406.
- [36] N. Savage, M.S. Diallo, Nanomaterials and water purification: opportunities and challenges, *Journal of Nanoparticle Research* 7 (4–5) (2005) 331–342.
- [37] Y. Sim, C.V. Chrysikopoulos, Three-dimensional analytical models for virus transport in saturated porous media, *Transport in Porous Media* 30 (1) (1998) 87–112.
- [38] E.D. Skouras, V.N. Burganos, C.A. Paraskeva, A.C. Payatakes, Simulation of the dynamic behavior of horizontal granular filters, *Separation and Purification Technology* 56 (3) (2007) 325–339.
- [39] K.E. Thompson, C.S. Willson, W.L. Zhang, Quantitative computer reconstruction of particulate materials from microtomography images, *Powder Technology* 163 (3) (2006) 169–182.
- [40] N. Tufenkji, M. Elimelech, Correlation equation for predicting single-collector efficiency in physicochemical filtration in saturated porous media, *Environmental Science & Technology* 38 (2004) 529–536.
- [41] R.E. Walpole, R.H. Myers, *Probability and Statistics for Engineers and Scientists*, 5th ed., Macmillan Publishing Company, New York, 1993.
- [42] D. Wildenschild, J.W. Hopmans, C.M.P. Vaz, M.L. Rivers, D. Rikard, B.S.B. Christensen, Using X-ray computed tomography in hydrology: systems, resolutions, and limitations, *Journal of Hydrology* 267 (3–4) (2002) 285–297.
- [43] D. Wolf-Gladrow, A Lattice-Boltzmann equation for diffusion, *Journal of Statistical Physics* 79 (5/6) (1995) 1023–1032.
- [44] K.M. Yao, Influence of suspended particle size on the transport aspect of water filtration, PhD thesis, University of North Carolina at Chapel Hill, 1968.
- [45] K.M. Yao, M.M. Habibian, C.R. O'Melia, Water and waste water filtration—concepts and applications, *Environmental Science & Technology* 5 (1971) 1105.
- [46] D. Zhang, R. Zhang, S. Chen, W.E. Soll, Pore scale study of flow in porous media: scale dependency, REV, and statistical REV, *Geophysical Research Letters* 27 (B) (2000) 1195–1198.
- [47] W.X. Zhang, Nanoscale iron particles for environmental remediation: an overview, *Journal of Nanoparticle Research* 5 (3–4) (2003) 323–332.